

Microscopic diamond Solid-Immersion-Lenses fabricated around single defect centers by focussed ion beam milling

Mohammad Jamali,¹ Ilja Gerhardt,^{1,2} Mohammad Rezaei,¹ Karsten Frenner,³ Helmut Fedder,¹ and Jörg Wrachtrup^{1,2}

¹⁾*3. Physikalisches Institut and Stuttgart Research Center of Photonic Engineering (SCoPE), Universität Stuttgart, Pfaffenwaldring 57, Stuttgart D-70569, Germany*

²⁾*Max Planck Institute for Solid State Research, Heisenbergstraße 1, D-70569 Stuttgart, Germany*

³⁾*Institute for technical optics (ITO), Universität Stuttgart, Pfaffenwaldring 7, Stuttgart D-70569, Germany*

(Dated: 13 October 2014)

Recent efforts to define microscopic solid-immersion-lenses (SIL) by focused ion beam milling into diamond substrates that are registered to a preselected single photon emitter are summarized. We show how we determine the position of a single emitter with at least 100 nm lateral and 500 nm axial accuracy, and how the milling procedure is optimized. The characteristics of a single emitter, a Nitrogen Vacancy (NV) center in diamond, are measured before and after producing the SIL and compared with each other. A count rate of 1.0 million counts per second is achieved with a [111] oriented NV center.

I. INTRODUCTION

Single optical emitters embedded in solid state materials are on the research horizon for more than twenty years¹. Not only their single photon emission, but also their nanoscopic size, and their properties as single optical and magnetic qubits allow for various quantum optics, quantum information and sensing experiments. Among them, color centers in diamond especially the negatively charged nitrogen vacancy (NV) center emerges as one of the promising candidates. It has a strong optical transition at 637 nm and local electron and nuclear spins with long spin coherence times even at room temperature that are suitable for quantum memories. Therefore, it has been used in different applications, such as quantum registers, magnetic field sensors and diamond-based single photon sources²⁻⁶.

Generally, a solid state environment allows for high collection efficiencies^{7,8}. The acceptance angle into the collection optics can be very high, and high refractive index allows for a small focus size. Various methods to increase collection efficiency have been proposed and experimentally studied⁹. Among them, thin layers⁸, pillar structures¹⁰, and solid immersion lenses (SILs) have been explored¹¹. A solid immersion lens increases the collection efficiency from a single emitter, by circumventing refraction from interfaces and thereby increasing the numerical aperture. Different geometries, namely the hemispherical SIL and the Weierstrass SIL have been researched⁹. The later is not optimal for spectrally broad emitters, since the shape results in strong chromatic aberrations. Hemispherical solid immersion lenses have been successfully used in single emitter studies, e.g. with single molecules¹², quantum dots¹³ and single defects in solids¹⁴⁻¹⁶.

Using a SIL for luminescent defects in diamond is especially interesting, since diamond has one of the highest refractive indices in the visible range ($n_d = 2.42$). The refractive index difference at the diamond-air interface causes strong refraction and total internal reflection (critical angle 24°) for the emitted light. Therefore, light emitted by a defect cannot be efficiently collected. Also for ideal spin properties, the NV defects under study should be embedded deeply in substrate¹⁷. Hence, it is important to fabricate special optical structures to enhance collection efficiency.

The approach of producing SILs directly on diamond started recently¹⁸. Two approaches have been established: To produce macroscopic half-spheres, with length scales of millimeters¹⁸, and to produce microscopic SILs in the order of several micrometers^{14,19}. Macroscopic

SILs were produced by laser and mechanical processing from small single crystalline CVD diamonds, which are overgrown on high quality high temperature high pressure (HPHT) grown diamond substrate. Microscopic SILs can be produced by focused ion beam (FIB) milling.

This paper outlines the microscopic manufacturing process for SILs. We describe the pathway to manufacture a solid immersion lens: first, a single emitter is optically located and characterized. Afterwards a SIL is manufactured around it. This is achieved by FIB milling. We compare different milling strategies and present the one that is optimal to produce SILs closest to the desired hemispherical shape and with least milling residuals.

II. LOCATING A SINGLE EMITTER

Before producing a SIL around a single emitter, we have to locate the emitter in all three spatial directions. Since these steps, the characterization under confocal microscopy and milling in the FIB machine, are performed in two different setups, it is required to introduce suitable marker structures that are visible in both microscopes and to which the position of the emitter and the SIL are referenced. This is required for lateral localization. For the localization in depth, we do not require a retrievable structure, since the surface serves as a reference.

We first discuss the lateral localization of the emitter: The localization accuracy of a single NV should be in the range of the field of view of the SIL. The field of view diameter, d_{FOV} , follows from a quarter-wave criterion²⁰ and is proportional to the square root of the SIL radius, r .

$$d_{FOV} < \sqrt{\frac{2r\lambda}{n(n-1)}}, \quad (1)$$

where λ is the optical wavelength and n is the refractive index of the SIL. For a 4 μm SIL in diamond and for $\lambda = 532 \text{ nm}$ this is about 1 μm . Consequently, the ability to locate an emitter, has to be significantly better than 1 μm , both in the FIB machine and the optical microscope.

We locate the emitter by measuring its relative position against three marker points in the confocal microscope, further we locate these points under the FIB and calculate the actual position of the NV. For this purpose we mill a rectangular pattern of cylindrical holes

(diameter 260 ± 20 nm, depth 500 nm, pitch $20 \mu\text{m}$, current 0.92 nA) into the sample with the FIB. These markers are well visible in the confocal fluorescence microscope (Fig.1a,b). It is currently not clear what is at the origin of their fluorescence. The fluorescence could either stem from graphitized material, implanted gallium or dirt contained in the immersion oil that is trapped inside the holes. Single emitters are laterally located by imaging the sample at the target emitter depth below the surface with a home-made confocal microscope (Fig.1c), including an oil-objective (Olympus, UPLANSAPO, $60\times$, 1.35 NA), single photon counting detectors and a 585 nm long-pass filter. The sample is mounted on a piezo scanner (PI, P-517.3CD with 1 nm in-plane and 0.1 nm vertical resolution). The excitation power was 0.5 mW onto the diffraction limited spot (600 nm). The imaging depth corresponds to the desired SIL radius, typically $2\text{-}6\mu\text{m}$ in the present case. Single emitters were identified by measuring the autocorrelation function in a Hanbury-Brown and Twiss configuration. After the emitters were located, the surface of the sample was imaged to locate the position of the three holes around the NV accurately. The accuracy of fabricated SIL is limited by the accuracy of locating markers in both experimental configurations. Since the optical signal from a single marker originates from a sub-wavelength structure, the accuracy for locating an ideal point source σ_r is in theory on the order of $\sigma_r \sim 0.61\lambda/(N.A.\sqrt{N})$, where N is the number of detected photons. This amounts to $\sim 1\text{nm}/\sqrt{\text{Hz}}$ for a single emitter with a detected count rate of 100 kcounts/s. For non-ideal spherical sources, such as the present alignment markers or for non-axial dipoles such as the single emitters in the present case, the localization accuracy is lower. The alignment accuracy is further limited by a (possibly inhomogeneous) fluorescence background and drift as well as imperfect repeatability of the piezo scanner. To examine the accuracy of this alignment procedure, we made the following test. First, we identified a specific emitter, then three markers around it were selected and all coordinates were recorded. As next step, the procedure was repeated and the coordinates of the same markers and emitter were recorded again. Finally, the expected coordinates of the emitter were calculated from the previous coordinates of the emitter and the previous and new coordinates of the markers. This procedure is identical to the calculation of the target SIL position from the ion beam image. The difference between the calculated and the measured new position of the emitter defines roughly the positioning accuracy which was typically better than 100 nm. In fact, by minimizing mechanical drift and fitting the experimental data with a Gaussian function it should be possible to achieve positioning accuracy of several

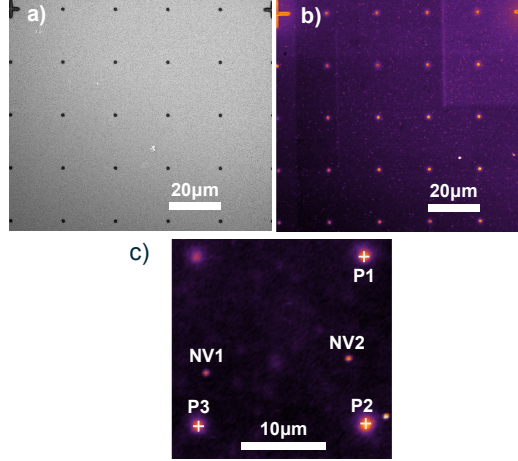


FIG. 1. a) SEM image of focused ion beam generated markers in a rectangular pattern of $20 \times 20 \mu\text{m}$. Pixel size: 120 nm. b) Optical image of the same markers, acquired in a confocal microscope. Pixel size: 200 nm. c) Confocal image of Sample showing two NVs and the markers around them. Note that the markers appear larger since the focal plane coincides with the NVs such that the markers are out of focus.

nanometers^{21,22}. As there was no need for such a accuracy in our experiment, the positions of the markers were extracted directly from the brightest pixels in the image.

The lateral coordinates r'_e of the emitter in the ion image follow from the coordinates of the emitter r_e and the coordinates of the markers r_0, r_1, r_2 in the optical image and the coordinates of the same markers r'_0, r'_1, r'_2 in the ion image as

$$r'_e = r'_0 + V'V^{-1}(r_e - r_0), \quad (2)$$

where the rows of the 2×2 matrices V and V' are $r_1 - r_0$ and $r_2 - r_0$, respectively $r'_1 - r'_0$ and $r'_2 - r'_0$.

After discussing the lateral localization of the emitter, we now turn to the depth determination. Optically, this is not a trivial task, since the refractive index mismatch between the immersion oil and the diamond elongates the effective focal length of the microscope objective and distorts its point spread function. Consider the extremal rays, which are given by the numerical aperture of the objective lens as shown in Fig. 2a). The depth of the emitter d follows from the displacement d_0 of the piezo stage as $d = d_0 \tan \theta_0 / \tan \theta$, where $\theta = \arcsin(\frac{n_0}{n} \sin \theta_0)$ and $n_0 \sin \theta_0 = N.A.$, where n_0 is the refractive index of the surrounding medium and θ_0 is the half opening angle. It is obvious that every ray bundle in the light

cone results in a different focal shift. This is a well known problem in confocal microscopy studied both experimentally^{23,24} and theoretically²⁵. For low numerical aperture lenses and small refractive index mismatch the estimate based on the extremal rays is reportedly a good approximation^{23,25}. With high numerical aperture lenses this approximation should be replaced by a wave optical treatment and the distorted point spread function should be computed. The intensity maximum of the point spread function (PSF) would then be identified with the apparent focus position. Note that in the present case of confocal fluorescence microscopy of a single emitter a number of additional effects should be taken into account, including both the illuminating and the emitting field (532 nm and 650-750 nm, respectively, in the present case), which are additionally effected by chromatic aberrations, the pinhole, and the emission pattern, determined by two perpendicular dipoles in case of the NV center. Moreover, in the present case the refractive index mismatch between the immersion oil ($n_{oil} = 1.52$) and diamond is exceptionally large. Note that in a full wave model, the effective depth will also no longer depend linearly on the nominal depth. Generally, as the PSF gets more and more distorted and the imaging quality is reduced, the objective lens effectively behaves like a lens with smaller numerical aperture. Or, equivalently, the extremal rays will no longer result in constructive interference and contribute less. We now perform two rough estimates to account for these effects: on the one hand, we consider the effective depth corresponding to the mean opening angle, given by $\bar{\theta} = 0.5 \arcsin(N.A./n)$. On the other hand, we evaluate the effective depth averaged over all rays that impinge on the back aperture of the objective with equal weight. The latter corresponds to a simple ray tracing model. In the present case, we obtain a correction factor $d'/d = \gamma = 1.80$ and $\gamma = 2.42$, for the prior and the latter estimate, respectively. We have also checked these results by full wave optical simulations of the three-dimensional PSF using Zemax, assuming an ideal objective lens with the same $N.A.$ as the one used in experiments. In this approach we used the same wavelength (650 nm) for illumination and emission and disregarded the confocal pinhole. These simulations confirmed that the conversion factor is depth dependent and in the range $\gamma \in [2.10, 1.95]$ for $d_0 \in [0, 10] \mu\text{m}$. For the experiments $\gamma = 1.85$ was used, which led to good results. While not being subject of the present study one could extend on this. The effective focus depth could be determined experimentally as follows. Consider a diamond sample with a thin (few nm) fluorescent layer at a depth several micrometers below the sample surface (such a sample could be created e.g. by CVD growth and delta doping²⁶

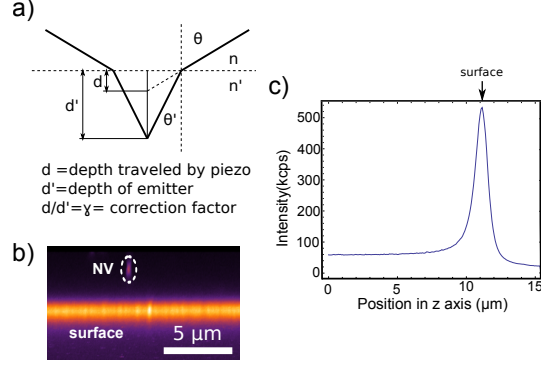


FIG. 2. a) Schematic of the focal shift in a high refractive index sample. b) Confocal scan of sample in xz plane. c) Intensity profile in z direction.

or by overgrowing a substrate with a 'dirty' initial surface). Next a staircase structure with well calibrated step height could be milled into the diamond down to the fluorescent layer by FIB. By measuring the effective depth of the fluorescent layer on all steps, the depth dependent effective focus could be reconstructed.

The other crucial factor for the depth determination is to locate the sample surface precisely. For this purpose we obtained a x-z scan through the sample (Fig.2b). The confocal image shows a bright band with a narrow line of higher intensity at its center, also the plot of the z position versus the intensity of the light shows a sharp peak which is related to the surface (Fig.2c). Our experimental results prove that our accuracy in depth determination is better than $1 \mu\text{m}$.

We produce hemispherical SILs with the radius equal to the depth of the NV, and a cone surrounding the SIL (Fig.4). The cone is chosen slightly larger than the acceptance cone of the microscope objective, such that the largest possible amount of light can be captured. More specifically, we use a cone radius slightly larger than

$$\frac{R_{\text{cone}}}{R_{\text{SIL}}} = \tan(\arcsin(\frac{N.A.}{n'})), \quad (3)$$

where n' is the refractive index of the diamond. This ratio is equal to 2.1 for the oil objective with the N.A. of 1.35.

III. FIB MILLING

Prior to milling the sample was mounted on a conductive holder with conducting silver paste and covered with 20 nm conductive gold. Subsequently the sample is placed inside the FIB machine and aligned by electron microscopy (EM). Before milling, astigmatism of the ion beam was carefully aligned in a prior step to optimize the beam shape.

FIB milling was performed on an FEI, Helios 400 machine using a so-called stream-file input. This file-format is machine-specific and contains milling times and x and y coordinates. We wrote scripts in the python programming language to generate stream file from NV and markers positions, that we include in the supplementary material. The programs use the width of the FIB image as a reference to calculate the relative coordinates of the structure. The milling time for each point is computed based on the given milling rate and the beam current that is used for the milling.

To define a hemisphere along with a conical cutout, we milled concentric rings with decreasing inner and outer diameter. Within each ring, we steer the beam on a double spiral beam path (two interleaved spirals with opposite handedness; see also supplementary source code) with equidistant points and we adjust the milling times of the edge points to account for the spherical shape. Note that a single spiral should yield comparable results. The number of rings (layers) varies depending on the beam current and size of the SIL. We ensure that the thickness of each milling layer is much smaller than the optical wavelength. To ensure homogeneous milling and at the same time keep the memory usage in the machine within the limits, each layer may comprise several repetitions of the same path. We also tested milling with automated drift correction, however, this did not effect on the quality of the SILs.

With these settings, first the alignment holes are milled as described above. After this milling, the sample is sonicated in acetone for 10 min to remove silver paste that was used for mounting the sample. Then the sample is cleaned in aqua regis to dissolve the evaporated gold layer. Furthermore the sample was cleaned in piranha solution, mixture of 1:1 concentrated sulfuric acid and 30 % hydrogen peroxide solution, to remove the organic material from surface and finally, rinsed in deionized water.

There are generally two milling strategies to define a 3D structure as we illustrate schematically in Fig. 3). In a first strategy, N identical milling layers are used. Each milling layer

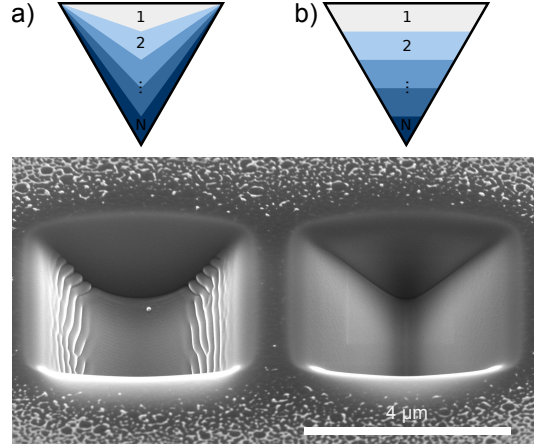


FIG. 3. Milling strategy for better focus and less residual. a) Same path, as shown schematically, was repetitively applied to the sample to mill a structure. The tip of the structure is round and there are visible residuals in both side walls. b) Different approach to mill the same structure: as shown schematically different milling paths were applied layer by layer. The sharpness is increased and no residuals are visible on the substrate.

covers the entire area of the structure and for each milling layer, the depth at each x - y -coordinate is $z(x, y)/N$. In a second strategy, the structure is sliced into N layers of equal thickness N/z_{max} (where z_{max} is the deepest point of the structure). The layers cover different areas and are milled successively, starting with the layer that covers the largest area. In the present case, it was crucial to use the latter strategy. The effect can be seen with a V-groove as a test structure. As is shown in Fig. 3, the first milling strategy results in significant broadening and milling residuals. By contrast, the second milling strategy produces a better result. In this case, the rounding of the dip is roughly given by the beam waist. For all milled SILs the second milling strategy was used.

The markers, which were previously located with confocal microscopy, were imaged by EM and FIB with lateral resolution of about 30 nm. After the determination of the marker coordinates in the FIB image, the relative position of the target NV is calculated in the FIB coordinates and a stream file for a SIL with radius coinciding with the NV depth is executed using the calculated lateral NV coordinate as origin. A typical set of milling parameters for a 10 μm SIL is outlined in Table I. One of the crucial values is the milling rate. To calibrate this rate we drilled a cylindrical structure on the sample with the known diameter, milling time and beam current. After milling, the depth of the cylinder was measured under 52°

TABLE I. FIB parameters

Parameter	value for 10 μm SIL
width of FIB image	64 μm
milling rate	0.21 $\frac{\mu\text{m}^3}{\mu\text{s}\cdot\text{nA}}$
beam current	2.7 nA
radius (SIL)	5 μm
radius (cone)	2.2·radius (SIL)
number of slices	100

angle by the SEM to calculate the volume of milled area. Some of the generated stream files have a length of 12.8 million points to be cut. The FIB only allows for a maximum number of 8 million points per file. To overcome this limitation, stream files were automatically split into several files. The produced files can be loaded into the machine at the same time and ran automatically after each other. The total milling time for the given example is 62 minutes and 55 seconds. The SEM image of the milled SIL is shown in Fig. 4a). After the milling process, the SIL is characterized in the EM. The presented SIL is a typical example and shows the quality and the overall deviations of the structure from the ideal shape. The surface roughness is determined to be on the order of 30 nm peak-to-valley, which was determined by SEM. In early experiments we milled cross sections through the SIL and carefully checked the spherical shape. The present stream files do not require any further corrections regarding the spherical shape of the SILs. Before any further optical characterization, the cleaning processes as explained before was applied. Additionally, the sample was boiled 3 hours in the mixture of concentrated sulphuric acid, nitric acid and perchloric acid in a volume ratio 1:1:1 to remove the residual materials and implanted gallium. While this cleaning procedure removes all background fluorescence, likely there is still implanted gallium present within the first 10 nanometers underneath the diamond surface²⁷.

IV. OPTICAL CHARACTERIZATION

The resulting SILs were characterized optically in a confocal fluorescence microscope. For our studies, we used a [111] cut diamond and a single NV center oriented perpendicular

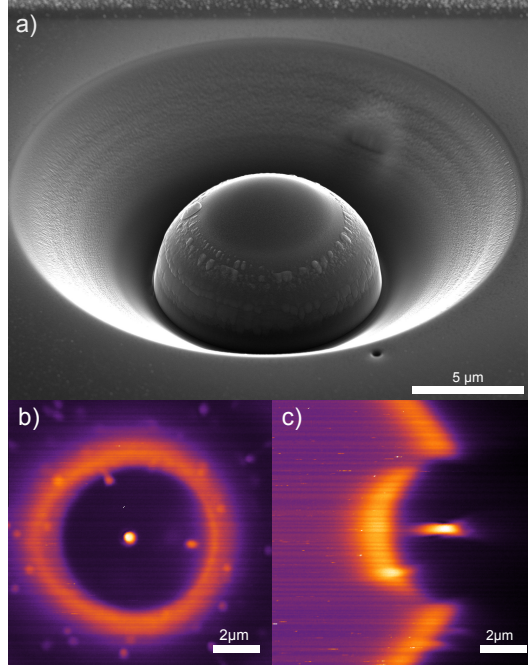


FIG. 4. SEM and optical characterization of the milled SIL. a) SEM image under 52° angle. b,c) Confocal images of the SIL with the NV center in the lateral and cross sectional plane respectively.

to the diamond surface. In this case, the two optical dipoles are oriented parallel to the surface, resulting in an optimal directivity of the dipolar emission pattern. Since we have studied all emitters prior to FIB-milling, it is possible to compare the results prior and after the milling process. The central aim is to optimize the detectable count-rates. Optical studies after milling are presented in Fig. 4b) and c). The deviation of the emitter from the center of the SIL is less than 150 nm. The PSF is found to be circular. In the linear excitation regime, the signal to background ratio is larger than 30. At higher laser powers, the background dominates, since it rises linearly with excitation power, while the single emitter is saturated. A saturated count rate of 1.0 Mcounts/s was observed, utilizing an oil objective (Fig. 5a), which is the highest count rate reported for a single NV in a bulk diamond so far. Compared to the saturated count rate without the SIL, 350 kcounts/s (data not shown), this is an enhancement $\xi = 3.4$. This agrees well with the expected enhancement

$$\xi = \frac{1 - \cos(\arcsin(N.A./n))}{1 - \cos(\arcsin(N.A./n'))} = 3.3. \quad (4)$$

Here n and n' are the refractive indices of the oil and diamond, respectively. The optical characterization was repeated with an air objective (Nikon, CFI LU Plan Fluor EPI P 100 \times , 0.9 NA), where we observed count rates of 65 kcounts/s and 600 kcounts/s, without and with

the SIL, respectively. Based on the specified numerical apertures, the collection angle of the oil and air objectives should be the same. This substantial difference in count rate cannot be explained by the increase of the reflection losses at the air-diamond interface, which is less than 10%. A possible explanation for this observation could be slight deviations of the SIL from the ideal hemispherical shape that are less critical when using an oil objective. A second explanation could be that there are substantial differences of the optical wave fronts, even though the manufacturers specify equivalent collection angles.

The acquired antibunching curve⁵ (see inset in Fig. 5a) clearly shows that we have a single emitter. The presented $g^{(2)}(\tau)$ -function was background corrected as outlined in literature²⁸. It further allows to estimate the decay rates of the excited state and metastable triplet state of the NV center. We find the following rates: $T_1 = 9$ ns, $T_m = 236$ ns, which is in good agreement with previous studies. To quantify the achievable count rate, we measure a saturation curve shown Fig. 5a). The low intensity part of the data is well described by

$$I_{em} = I_{inf} \frac{I_0}{I_0 + I_{sat}}, \quad (5)$$

where I_{em} is the emitted intensity, I_0 is the incident intensity, I_{sat} is the saturation intensity and I_{inf} is the saturated fluorescence intensity. The above model commonly describes a two-level system, a three-level system with a long lived metastable singlet level, a five-level system accounting for the different spin states of the NV center, as well as a simple four-level system accounting for optically induced charge state switching between NV^0 and NV^{-} ²⁹. With realistic parameters, all of these models result in qualitatively the same saturation curve. However, at high excitation powers, these models fail to describe the present data. Indeed, in our data we observe that the fluorescence decreases towards high incident powers. Such behaviour has been reported previously^{18,30} and was attributed to the existence of dark states that could be described by a six-level system. Here we propose two simpler models that allow us to describe the saturation behavior at high incident powers. Note that similar models have been exploited to explain the population dynamics of molecules, chromium³¹ and SiV³² centers in diamond. The models are shown schematically in Fig.5 b) and c). We assume that there exists a higher lying excited state that is populated optically and decays spontaneously either back to the same state or to the ground state, indicated by the dashed arrows (within the limits considered below, both cases result in the same saturation behaviour). The higher lying excited state behaves like a shelving state. Note that it is

key that the decay of the higher lying state is spontaneous. This is in contrast to the NV^- to NV^0 switching mechanism, where both the ionization and the recovery path are believed to be driven by optical pumping²⁹. The higher lying state could be coupled either to the excited state or to the metastable singlet state. Thus, the first model employs a three-level system with ground and excited state and an additional higher lying excited state that can be populated optically from the lower excited state and decays spontaneously (the meta stable state is omitted here, to provide the simplest possible model). The second model employs a four-level system with ground, excited and metastable singlet state and a higher lying excited state that can be populated from the singlet state and decays spontaneously back to the singlet state. The models are characterized by the transition rates between the states, which are the excitation and emission rates between the ground and excited state, the excitation and recovery rates to and from the higher lying state and the population and decay rate of metastable state. The rates are denoted γ_{ex} , γ_{em} , γ_{sh} , γ_{re} , γ_p , and γ_d , respectively. The excitation rates are proportional to the incident intensity and the corresponding efficiencies: $\gamma_{ex}(I_0) = \eta_{ex}I_0$ and $\gamma_{sh}(I_0) = \eta_{sh}I_0$. The corresponding rate equations result in saturation curves

$$I_{em} \propto \frac{\gamma_{re}\eta_{ex}I_0}{\gamma_{em}\gamma_{re} + \gamma_{re}\eta_{ex}I_0 + \eta_{ex}\eta_{sh}I_0^2} \quad (6)$$

and

$$I_{em} \propto \frac{\gamma_d\gamma_{re}\eta_{ex}I_0}{(\gamma_p + \gamma_{em})\gamma_d\gamma_{re} + (\gamma_p + \gamma_d)\gamma_{re}\eta_{ex}I_0 + \gamma_p\eta_{ex}\eta_{sh}I_0^2} \quad (7)$$

for the three- and four-level model, respectively. Both models result in the same expression for the saturation curve with three free constants. We fit the experimental data with this common expression. The result is shown by the blue curve in Fig.5.

We conjecture that quite generally, the introduction of a higher lying excited state that is populated by optical pumping but that decays spontaneously will result in the observed saturation behavior.

V. CONCLUSION

In this paper, we describe our procedure to precisely locate single emitters both optically inside a diamond substrate and in a focused ion beam machine. FIB milled holes have proven suitable alignment markers, providing 100 nm lateral and 500 nm axial accuracy. We have compared different FIB milling strategies. Milling layers of equal thickness yielded the best

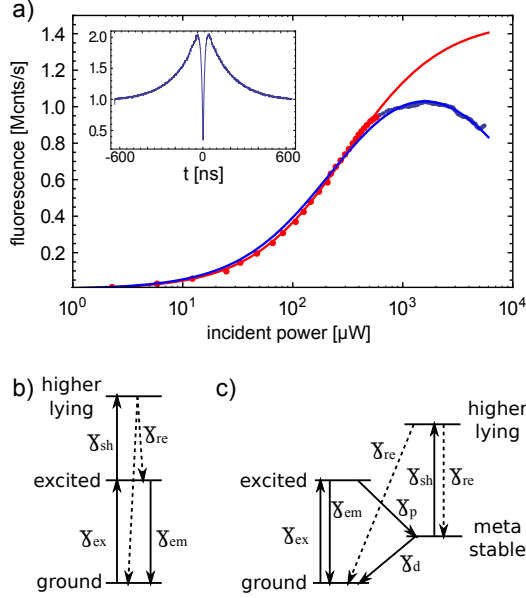


FIG. 5. Saturation behaviour. a) The saturation curve of NV in the center of the SIL (red and blue dots), The red dots show the data up to $550 \mu\text{W}$, the blue dots show the full data set. The red and blue line show fits with a two-level model and a three-level model with higher lying excited state, respectively (see text for details). The inserted plot shows the antibunching at high laser power. b),c) Three- and four-level rate equation models with spontaneously decaying higher lying excited states.

result. This strategy might be applied to other hard materials, to ensure a minimal amount of residuals and optimal feature sharpness. We present record-high count rates of NV at the focus of a SIL. The technique paves the way for high-brightness single photon sources based on solid state emitters and novel spin-control schemes.

ACKNOWLEDGMENTS

We thank Florian Dolde and Samuel Wagner for help with spin measurements in the SILs and Sen Yang, Thai-Hien Tran and Andrej Denisenko for fruitful discussions. The hospitality of the ITO, Stuttgart is acknowledged. We acknowledge financial support by the Max Planck Society, the ERC project SQUTEC, the DFG SFB/TR21, the EU projects DIAMANT, SIQS, QESSENCE and QINVC, the JST-DFG (FOR1482 and FOR1493), the Volkswagenstiftung and the Landesstiftung Baden-württemberg.

REFERENCES

- ¹W. E. Moerner and L. Kador, *Phys. Rev. Lett.* **62**, 2535 (1989).
- ²F. Jelezko and J. Wrachtrup, *physica status solidi a* **203**, 3207 (2006).
- ³M. V. G. Dutt, L. Childress, L. Jiang, E. Togan, J. Maze, F. Jelezko, A. S. Zibrov, P. R. Hemmer, and M. D. Lukin, *Science* **316**, 1312 (2007).
- ⁴R. Brouri, A. Beveratos, J.-P. Poizat, and P. Grangier, *Opt. Lett.* **25**, 1294 (2000).
- ⁵C. Kurtsiefer, S. Mayer, P. Zarda, and H. Weinfurter, *Phys. Rev. Lett.* **85**, 290 (2000).
- ⁶G. Balasubramanian, I. Y. Chan, R. Kolesov, M. Al-Hmoud, J. Tisler, C. Shin, C. Kim, A. Wojcik, P. R. Hemmer, A. Krueger, T. Hanke, A. Leitenstorfer, R. Bratschitsch, F. Jelezko, and J. Wrachtrup, *Nature* **455**, 648 (2008).
- ⁷K. Koyama, M. Yoshita, M. Baba, T. Suemoto, and H. Akiyama, *Applied Physics Letters* **75**, 1667 (1999).
- ⁸K. Lee, X. Chen, E. H., K. P., R. Lettow, A. Renn, V. Sandoghdar, and S. Gotzinger, *Nat Photon* **5**, 166 (2011).
- ⁹W. Barnes, G. Björk, J. Gérard, P. Jonsson, J. Wasey, P. Worthing, and V. Zwiller, *Eur. Phys. J. D* **18**, 197 (2002).
- ¹⁰T. M. Babinec, H. J. M., M. Khan, Y. Zhang, J. R. Maze, P. R. Hemmer, and M. Loncar, *Nat Nano* **5**, 195 (2010).
- ¹¹S. M. Mansfield and G. S. Kino, *Applied Physics Letters* **57**, 2615 (1990).
- ¹²G. Wrigge, I. Gerhardt, J. Hwang, G. Zumofen, and V. Sandoghdar, *Nat Phys* **4**, 60 (2008).
- ¹³A. N. Vamivakas, M. Atatuere, J. Dreiser, S. T. Yilmaz, A. Badolato, A. K. Swan, B. B. Goldberg, A. Imamoglu, and M. S. Unlu, *Nano Letters* **7**, 2892 (2007), <http://pubs.acs.org/doi/pdf/10.1021/nl0717255>.
- ¹⁴L. Robledo, L. Childress, H. Bernien, B. Hensen, P. F. A. Alkemade, and R. Hanson, *Nature* **477**, 574 (2011).
- ¹⁵G. Waldherr, Y. Wang, S. Zaiser, M. Jamali, T. Schulte-Herbrüggen, H. Abe, T. Ohshima, J. Isoya, J. F. Du, P. Neumann, and J. Wrachtrup, *Nature* **506**, 204 (2014).
- ¹⁶R. Kolesov, K. Xia, R. Reuter, M. Jamali, R. Stöhr, T. Inal, P. Siyushev, and J. Wrachtrup, *Phys. Rev. Lett.* **111**, 120502 (2013).

- ¹⁷B. Naydenov, F. Dolde, L. T. Hall, C. Shin, H. Fedder, L. C. L. Hollenberg, F. Jelezko, and J. Wrachtrup, *Phys. Rev. B* **83**, 081201 (2011).
- ¹⁸P. Siyushev, F. Kaiser, V. Jacques, I. Gerhardt, S. Bischof, H. Fedder, J. Dodson, M. Markham, D. Twitchen, F. Jelezko, and J. Wrachtrup, *Applied Physics Letters* **97**, 241902 (2010).
- ¹⁹L. Marseglia, J. P. Hadden, A. C. Stanley-Clarke, J. P. Harrison, B. Patton, Y.-L. D. Ho, B. Naydenov, F. Jelezko, J. Meijer, P. R. Dolan, J. M. Smith, J. G. Rarity, and J. L. O'Brien, *Applied Physics Letters* **98**, 133107 (2011).
- ²⁰M. Baba, T. Sasaki, M. Yoshita, and H. Akiyama, *Journal of Applied Physics* **85**, 6923 (1999).
- ²¹N. Bobroff, *Review of Scientific Instruments* **57**, 1152 (1986).
- ²²R. E. Thompson, D. R. Larson, and W. W. Webb, *Biophysical Journal* **82**, 2775 (2002).
- ²³K. Carlsson, *Journal of Microscopy* **163**, 167 (1991).
- ²⁴S. Hell, G. Reiner, C. Cremer, and E. H. K. Stelzer, *Journal of Microscopy* **169**, 391 (1993).
- ²⁵T. D. Visser, J. L. Oud, and G. J. Brakenhoff, *Optik* **90**, 17 (1992).
- ²⁶K. Ohno, F. Joseph Heremans, L. C. Bassett, B. A. Myers, D. M. Toyli, A. C. Bleszynski Jayich, C. J. Palmstrøm, and D. D. Awschalom, *Applied Physics Letters* **101**, 082413 (2012).
- ²⁷M. Widmann, S.-Y. Lee, T. Rendler, N. T. Son, H. Fedder, S. Paik, N. Zhao, S. Yang, I. Booker, A. Denisenko, M. Jamali, S. A. Momenzadeh, T. Ohshima, A. Gali, E. Janzén, and J. Wrachtrup, *arXiv:1407.0180 [cond-mat]* (2014), arXiv: 1407.0180.
- ²⁸S. C. Kitson, P. Jonsson, J. G. Rarity, and P. R. Tapster, *Phys. Rev. A* **58**, 620 (1998).
- ²⁹K. Beha, a. Batalov, N. B. Manson, R. Bratschitsch, and a. Leitenstorfer, *Physical Review Letters* **109**, 097404 (2012).
- ³⁰K. Y. Han, D. Wildanger, E. Rittweger, J. Meijer, S. Pezzagna, S. W. Hell, and C. Eggeling, *New Journal of Physics* **14**, 123002 (2012).
- ³¹I. Aharonovich, S. Castelletto, D. a. Simpson, a. D. Greentree, and S. Prawer, *Physical Review A* **81**, 1 (2010).
- ³²E. Neu, M. Agio, and C. Becher, *Optics express* **20**, 19956 (2012), arXiv:1107.0502.